

A quantitative theory for heterogeneous combustion of nonvolatile metal particles in the diffusion-limited regime

Daoguan Ning, Andreas Dreizler

Reactive Flows and Diagnostics, Department of Mechanical Engineering, Technical University of Darmstadt, Otto-Berndt-Str. 3, 64287 Darmstadt, Germany

Abstract

The paper presents an analytical theory quantitatively describing the heterogeneous combustion of nonvolatile (metal) particles in the diffusion-limited regime. It is assumed that the particle is suspended in an unconfined, isobaric, quiescent gaseous mixture and the chemisorption of the oxygen takes place evenly on the particle surface. The exact solution of the particle burn time is derived from the conservation equations of the gas-phase described in a spherical coordinate system with the utilization of constant thermophysical properties, evaluated at a reference film layer. This solution inherently takes the Stefan flow into account. The approximate expression of the time-dependent particle temperature is solved from the conservation of the particle enthalpy by neglecting the higher order terms in the Taylor expansion of the product of the transient particle density and diameter squared. Coupling the solutions for the burn time and time-dependent particle temperature provides quantitative results when initial and boundary conditions are specified. The theory is employed to predict the burn time and temperature of micro-sized iron particles, which are then compared with measurements, as the first validation case. The theoretical burn time agrees with the experiments almost perfectly at both low and high oxygen levels. The calculated particle temperature matches the measurements fairly well at relatively low oxygen mole fractions, whereas the theory overpredicts the particle peak temperature due to the neglect of evaporation and the possible transition of the combustion regime.

Keywords: Analytical solution, Burn time, Temperature evolution,

Email address: ning@rsm.tu-darmstadt.de (Daoguan Ning)

Novelty and significance statement

For the first time, we present a comprehensive and quantitative analytical theory elucidating the heterogeneous combustion of nonvolatile (metal) particles in the diffusion-limited regime. This novel theoretical model exhibits a remarkable capacity for quantitative prediction, obviating the need for supplementary information from numerical simulations or experimental data. The derivation process of analytical solutions for burn time and time-dependent particle temperature from conservation equations is elaborated, offering transparency and insight into the model's foundations. To demonstrate the practical utility of the theory, we apply it to analyze the combustion of iron particles, providing valuable mathematical perspectives on the underlying processes. The model's predictions for burn time and temperature align closely with experimental results, offering a partial validation of the theory within the realm of its applicable assumptions. This pioneering work contributes a robust and versatile analytical framework, advancing our understanding of diffusion-limited combustion phenomena of nonvolatile particles.

CRedit authorship contribution statement

D. Ning: Conceptualization, Investigation, Methodology, Writing – original draft, review & editing. **A. Dreizler:** Funding acquisition, Project administration, Writing – review & editing.

1. Introduction

The combustion of nonvolatile metal particles or powders presents a promising strategy for achieving carbon-free conversion of clean energy on demand. Unlike the vapor-phase combustion observed in volatile droplets or the heterogeneous combustion of coal and biomass particles, where both mass and diameter typically decrease during combustion, nonvolatile metal particles exhibit a distinctly burning behavior. As the nonvolatile burning process progresses, the condense-phase reaction product accumulates within the particle, leading to an increase in both particle mass and diameter. This unconventional combustion feature deviates significantly from the established theories developed for vapor-phase or heterogeneous combustion of droplets and volatile particles, such as the classical d^2 -law [1], which originated from the vaporization of liquid droplets. When applied

to the scenario of nonvolatile particle combustion, these theories lack a rigorous physical foundation. Recognizing the deficiency in understanding the combustion of nonvolatile particles, recent years have witnessed a surge in research efforts. Iron particles, in particular, have garnered substantial attention, with numerous studies aimed at unraveling the intricacies of their combustion behavior. Other metals, like aluminium and silicon, are also expected to burn heterogeneously at elevated pressures and reduced oxygen mole fractions, where the boiling points of the metals exceed their combustion temperatures.

In experimental measurements, multiple concepts have been proposed to investigate the fundamentals of single iron particle combustion. Wright et al. [2] measured the burn time of single iron particles by injecting single particles, ranging in diameter from 30 to 60 μm , into preheated O_2/Ar mixtures at 1000 K and atmospheric pressure. It is observed that the particle burn time (defined as the time to peak luminosity) reduces as the oxygen concentration increases. Later, Ning et al. [3] further quantified the burn time of micron-sized iron particles, ignited by a focused laser beam and subsequently burning at room temperature. It is inferred that the combustion process from ignition to the peak temperature is limited by external oxygen diffusion, supported by the inverse proportionality between the burn time and the oxygen mole fraction in the ambient. Using the same particle generation and ignition apparatus, the evolution of the surface temperature and diameter during iron particle combustion were also quantified by Ning et al. [4]. The measurement revealed that particle diameter increases almost linearly with elevating particle temperature, reaching a plateau during the cooling phase. This observation suggests that a relatively rapid oxidation rate is sustained throughout the particle burn time, with further oxidation occurring at a significantly slower rate after the particle peaks in temperature. In addition to laser ignition accomplished at low gas temperature, the combustion of iron particles in hot environments provided by the exhaust of lean-premixed gaseous flames [5, 6, 7] or a drop-tube furnace [8] has been more extensively investigated. It is commonly observed that as the oxygen mole fraction increases, the burn time shortens, and simultaneously, the maximum particle temperature rises until a moderate oxygen level. These trends align with typical characteristics of particle combustion in the diffusion-dominated regime (but unnecessarily the diffusion-limited regime).

In numerical simulations, investigations into single iron particle combustion have been conducted from various perspectives, including particle-resolved modeling [9], the point-particle approximation [10, 11], and molecular-scale surface chemisorption [12]. Based on the assumption of the diffusion-limited combustion regime, Thijs et al. [9] performed quantitative modeling of burn time and

temperature for laser-ignited iron particles, corresponding to experimental setups [3, 13, 14]. The simulated burn time aligns well with measurements across a wide range of oxygen levels. However, calculated particle peak temperatures only match experimental results at relatively low oxygen mole fractions. At high oxygen levels, the numerical simulation tends to overestimate the experimental outcome. To account for this discrepancy, Fujinawa et al. [10] speculated that at relatively high oxygen levels, the rate-limiting mechanism for iron particle combustion may transition to the diffusion of ions in the liquid oxide layer. Employing reactive molecular dynamic simulations, Thijs et al. [12] demonstrated that the continuum model, constructed for the diffusion-limited regime, effectively describes the combustion behavior of iron particles with dimensions on the order of tens of microns up to the peak temperature not exceeding approximately 2500 K. This finding indicates that conservation equations with the continuum assumption remain applicable for the theoretical analysis of nonvolatile particle combustion, provided that the particle size is significantly larger than the mean free path, and the mass accommodation coefficient of the oxygen is close to unity.

In theoretical frameworks, analytical solutions offer a comprehensive overview of general problems, complementing experiments and numerical simulations to enhance our understanding. Unfortunately, the quest for justified analytical models with predictive capability and quantitative accuracy for nonvolatile particle combustion remains elusive, impeded by the complexity of solving the nonlinear differential equations governing the problem. Bidabadi and his collaborators [15, 16, 17] attempted theoretical analysis of single iron particle combustion using several mathematical approaches. However, these theoretical models were formulated on the basis of self-contradictory assumptions: 1) the oxidation rate, described by an Arrhenius-like expression, was assumed to be proportional to the particle surface area throughout the entire combustion process, a justification applicable only to the kinetic-limited regime; 2) the burn time was evaluated using an analytical solution derived for the lifetime of vapor-phase droplet combustion in the diffusion-limited regime [1]. Consequently, the results obtained from these models lack a rigorous physical justification. Accounting for the variation of particle diameter during oxidation, Hazenberg [18] derived an analytical solution for the burn time of nonvolatile particles in the diffusion-limited combustion regime. While the expression explicitly describes the dependence of burn time on other parameters, for the mass diffusivity of oxygen, it needs estimation from one-to-one numerical simulations or using measured particle temperatures from experiments [19]. Moreover, the model becomes less rigorous with increasing oxygen levels due to the neglect of Stefan flow. Therefore, there is a need to further develop

a comprehensive analytical theory for quantitatively predicting the combustion characteristics of nonvolatile particles in the diffusion-limited regime. This study aims to uncover the underlying objectives in this regard.

The paper is structured as follows. In Section 2, the interfacial heat and mass transfer rates are derived from the conservation equations of the gas phase considering relevant boundary conditions. Subsequently, the burn time of nonvolatile particle combustion in the diffusion-limited regime is formulated explicitly. The transient solution for the particle temperature is analytically solved using Taylor expansion and appropriate approximations. The coupling of the solutions for the burn time and time-averaged temperature of the particle yields quantitative results for defined boundary and initial conditions. In Section 3, the theory is applied to analyze the combustion of iron particles, considering various effects of particle and gas-phase properties. The theoretical results are then compared with experiments to validate the proposed theory. Finally, the main conclusions drawn from this study are summarized in Section 4.

2. Mathematical formulation and solutions

The problem being addressed is illustrated in Fig. 1. An isolated, spherical metal particle is suspended in a quiescent, isotropic, unconfined gaseous mixture. The ignition of the pure metal particle is simplified by initiating it at its ignition temperature. The subsequent nonvolatile combustion process is assumed to be limited by the external diffusion of the oxygen (i.e., the diffusion-limited regime), and the structure of the particle remains spherically symmetric, facilitating even chemisorption of the oxygen on the particle surface. During combustion, the heat generated by exothermic oxidation is transported outward, while the oxygen is transported inward. Meanwhile, the mass of the particle increases due to the incorporation of the oxygen, resulting in a growth of the particle size. As the particle temperature may exceed the melting points of the metal and oxide, the solid particle may transform into a liquid droplet consisting of both liquid metal and liquid oxide. Nevertheless, it will still be referred to as a particle in this context. For the sake of simplicity, the phase transitions of the particle are neglected, adopting constant specific heat. The temperature, T_g , and composition, Y_i , of the gas vary between the particle surface and the far-field as $r \rightarrow \infty$, where r is the radial coordinate. The combustion time and temperature history of the particle will be solved analytically.

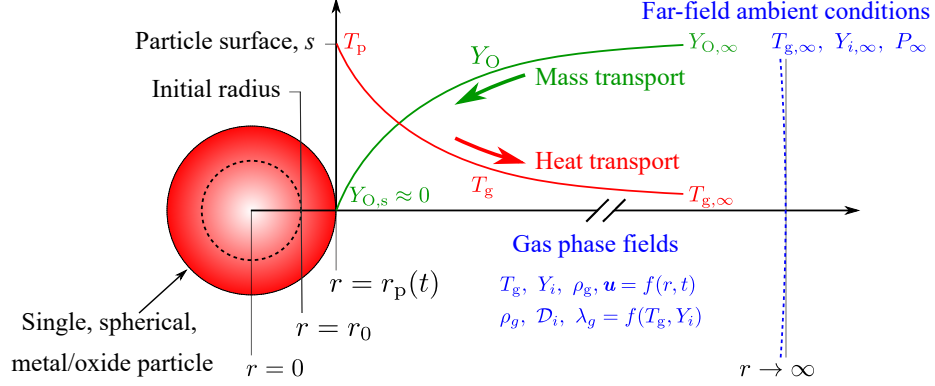


Figure 1: Schematic illustration of the combustion process for a single, non-volatile metal particle in the diffusion-limited regime.

2.1. Interfacial heat and mass transfer rates

During the combustion of non-volatile fuel particles, gas-phase reactions are absent and the combustion product is formed on the particle surface. Therefore, employing the quasi-steady-state assumption, the gas phase conservation equations for mass, the mass fraction of the oxygen, and energy are written in a spherical coordinate system as

$$\frac{\partial}{\partial r} \left(r^2 \rho_g \mathbf{u} \right) = 0, \quad (1)$$

$$\frac{\partial}{\partial r} \left(r^2 \rho_g \mathbf{u} Y_O \right) - \frac{\partial}{\partial r} \left(r^2 \rho_g \mathcal{D}_O \frac{\partial Y_O}{\partial r} \right) = 0, \quad (2)$$

$$\frac{\partial}{\partial r} \left(r^2 \rho_g \mathbf{u} h_g \right) - \frac{\partial}{\partial r} \left(r^2 \lambda_g \frac{\partial T_g}{\partial r} \right) - \frac{\partial}{\partial r} \left(\sum_{i=1}^N r^2 \rho_g \mathcal{D}_i h_i \frac{\partial Y_i}{\partial r} \right) = 0, \quad (3)$$

where ρ , \mathbf{u} , Y , \mathcal{D} , h , and λ represent the density, velocity, mass fraction, mass diffusion coefficient, specific enthalpy, and conductivity, respectively. The subscripts, g, O, and i denote the gas phase, oxygen, and individual species, respectively. N is the number of species in the gas phase. The boundary conditions at the particle

surface are

$$r = r_p : \begin{cases} \rho_g \mathcal{D}_O \frac{\partial Y_O}{\partial r} \Big|_s - \rho_g \mathbf{u}_s Y_{O,s} = \frac{\dot{m}_O}{4\pi r_p^2}, & (4a) \\ Y_O = Y_{O,s}, & (4b) \\ \lambda_g \frac{\partial T_g}{\partial r} \Big|_s = h_T (T_{g,\infty} - T_p) = \frac{\dot{Q}_{\text{conv}}}{4\pi r_p^2}, & (4c) \\ T_g = T_p, & (4d) \end{cases}$$

with \dot{m}_O being the mass consumption rate of the oxygen, h_T the heat transfer coefficient, and \dot{Q}_{conv} the convective heat transfer rate between the particle and the gas phase. The boundary conditions at the far-field read

$$r \rightarrow \infty : \begin{cases} Y_O = Y_{O,\infty}, & (5a) \\ T_g = T_{g,\infty}. & (5b) \end{cases}$$

To derive the interfacial heat and mass transfer rates, we will assume that the thermo-physical properties remain constant. This assumption is found to be satisfactory when the properties are evaluated at a virtual film layer with the reference conditions:

$$T_f := T_p + A_f (T_{g,\infty} - T_p), \quad (6)$$

and

$$Y_{O,f} := Y_{O,s} + A_f (Y_{O,\infty} - Y_{O,s}), \quad (7)$$

with A_f being the weighting coefficient, commonly taken as 1/3 [20].

We will first derive the interfacial mass transfer rate of the oxygen. Since only the oxygen has a net mass flux, integrating (1) from r_p to ∞ gives

$$r^2 \rho_g \mathbf{u} = -\frac{\dot{m}_O}{4\pi}, \quad (8)$$

where the negative sign indicates that \dot{m}_O is inward. Substituting (8) into (2) gives

$$\frac{\partial}{\partial r} \left(-\frac{\dot{m}_O}{4\pi} Y_O - r^2 \rho_g \mathcal{D}_O \frac{\partial Y_O}{\partial r} \right) = 0. \quad (9)$$

Integrating Eq. (9) from r_p to r , and applying the boundary condition (4a) yields

$$4\pi r^2 \rho_g \mathcal{D}_O \frac{dY_O}{dr} = \dot{m}_O (1 - Y_O). \quad (10)$$

Integrating Eq. (10) from r to ∞ yields

$$\ln\left(\frac{1 - Y_{O,\infty}}{1 - Y_O(r)}\right) = -\frac{1}{r} \frac{\dot{m}_O}{4\pi\rho_g\mathcal{D}_O}. \quad (11)$$

Applying the boundary condition (4b) to the above equation (10) gives the first expression for \dot{m}_O :

$$\dot{m}_O = -4\pi r_p \rho_g \mathcal{D}_O \ln(1 + B_M), \quad (12)$$

with B_M being the Spalding mass transfer number of the oxygen, defined analogously to that of vaporized fuel [21] as

$$B_M := \frac{Y_{O,\infty} - Y_{O,s}}{Y_{O,s} - 1}. \quad (13)$$

We introduce the Sherwood number, Sh , defined as

$$Sh := 2 \frac{\ln(1 + B_M)}{B_M}, \quad (14)$$

which inherently takes the Stefan flow effect into account. Except for the atmosphere with (nearly) pure oxygen [1, p. 506], in the diffusion-limited combustion regime:

$$Y_{O,s} \approx 0 \Rightarrow B_M \approx -Y_{O,\infty}. \quad (15)$$

Substituting (14) and (15) into (12) yields

$$\dot{m}_O = Sh\pi d_p \rho_g \mathcal{D}_O Y_{O,\infty} = -2\pi d_p \rho_g \mathcal{D}_O \ln(1 - Y_{O,\infty}). \quad (16)$$

The explicit expression of the interfacial heat transfer rate, \dot{Q}_{conv} , can be derived by following a similar procedure as for \dot{m}_O . We consider the facts that the net mass flux of each inert species is zero:

$$r^2 \rho_g \mathbf{u} Y_i - r^2 \rho_g \mathcal{D}_i \frac{\partial Y_i}{\partial r} = 0, \quad i \in [1, N] \ \& \ i \neq i_O \quad (17)$$

and the specific enthalpy of the gaseous mixture encompasses those of individual species:

$$h_g = \sum_{i=1}^N h_i Y_i = h_O Y_O + \sum_{i=1, i \neq i_O}^N h_i Y_i. \quad (18)$$

Substituting Eqs. (8), (10), (17) and (18) into Eq. (3) yields

$$\frac{\partial}{\partial r} \left(-\frac{\dot{m}_O}{4\pi} h_O - \lambda_g r^2 \frac{\partial T_g}{\partial r} \right) = 0. \quad (19)$$

Integrating Eq. (19) from r_p to r and applying the boundary condition (4c) gives

$$4\pi r^2 \lambda_g \frac{dT_g}{dr} = \dot{m}_O c_{p,O} \left(T_p - T_g + \frac{\dot{Q}_{\text{conv}}}{\dot{m}_O c_{p,O}} \right), \quad (20)$$

where the relation $h = c_p T$ has been used. Integrating Eq. (20) from r to ∞ gives T_g as a function of the radial distance:

$$\ln \left(\frac{T_p - T_{g,\infty} + \frac{\dot{Q}_{\text{conv}}}{\dot{m}_O c_{p,O}}}{T_p - T_g(r) + \frac{\dot{Q}_{\text{conv}}}{\dot{m}_O c_{p,O}}} \right) = -\frac{1}{r} \frac{\dot{m}_O c_{p,O}}{4\pi \lambda_g} \quad (21)$$

At $r = r_p$, Eq. (21) provides the second expression for \dot{m}_O :

$$\dot{m}_O = -4\pi r_p \frac{\lambda_g}{c_{p,O}} \ln(1 + B_T), \quad (22)$$

where B_T is the Spalding heat transfer number in our case, defined as

$$B_T := \frac{\dot{m}_O c_{p,O}}{\dot{Q}_{\text{conv}}} (T_p - T_{g,\infty}). \quad (23)$$

Substituting Eq. (22) into Eq. (23) yields

$$\dot{Q}_{\text{conv}} = 4\pi r_p \lambda_g \frac{\ln(1 + B_T)}{B_T} (T_{g,\infty} - T_p). \quad (24)$$

We introduce the Nusselt number, Nu , defined as

$$\text{Nu} := 2 \frac{\ln(1 + B_T)}{B_T}. \quad (25)$$

Substituting Eq. (25) into Eq. (24) gives

$$\dot{Q}_{\text{conv}} = \text{Nu} \pi d_p \lambda_g (T_{g,\infty} - T_p) \quad (26)$$

Finally, the two expressions for \dot{m}_O , i.e., Eqs. (12) and (22), relate B_T and B_M :

$$1 + B_T = (1 + B_M)^{\frac{1}{\text{Le}_O} \frac{c_{p,O}}{c_{p,g}}}, \quad (27)$$

where $\text{Le}_O = \lambda_g / (\rho_g c_{p,g} \mathcal{D}_O)$ is the Lewis number of the oxygen at the film layer. In the follows, the mass diffusivity of the oxygen and the thermal conductivity and specific heat of the gaseous mixture evaluated at the film layer will be denoted as $(\rho_g \mathcal{D}_O)_f$, λ_f , and $c_{p,f}$, respectively.

2.2. Analytical solution for particle burn time

During non-volatile combustion, the particle mass increases by consuming the oxygen, which is described as

$$\frac{dm_p}{dt} = \frac{\pi}{6} \frac{d(\rho_p d_p^3)}{dt} = \dot{m}_O, \quad (28)$$

with m_p and ρ_p being the time-dependent mass and density of the particle, respectively. As derived in [Appendix A](#) (see Supplementary Material), ρ_p is a function of the density of the metal, ρ_m , and that of the metal oxide, ρ_{mo} :

$$\rho_p = \rho_1 + \rho_2 \left(\frac{d_0}{d_p} \right)^3, \quad (29)$$

with

$$\rho_1 := \frac{\rho_{mo}}{s + (1-s)\varrho}, \quad (30)$$

and

$$\rho_2 := \frac{(\rho_m - \rho_{mo})s}{s + (1-s)\varrho}, \quad (31)$$

where s is the stoichiometric oxide-to-oxygen mass ratio, and ϱ is the oxide-to-metal density ratio. Substituting Eqs. (16) and (29) into Eq. (28) yields

$$\frac{d(\rho_1 d_p^3 + \rho_2 d_0^3)}{dt} = -12d_p (\rho_g \mathcal{D}_O)_f \ln(1 - Y_{O,\infty}). \quad (32)$$

Because $\rho_2 d_0^3$ is constant, Eq. (32) simplifies as

$$\rho_1 d_p \frac{d(d_p)}{dt} = -4 (\rho_g \mathcal{D}_O)_f \ln(1 - Y_{O,\infty}). \quad (33)$$

Integrating Eq. (33) from t_0 ($t_0 = 0$: $d_p = d_0$) to t ($t_0 \leq t \leq t_b$) gives the particle diameter evolution:

$$d_p^2 = d_0^2 - \frac{8 (\rho_g \mathcal{D}_O)_f \ln(1 - Y_{O,\infty})}{\rho_1} t. \quad (34)$$

where d_0 is the initial particle diameter. Since the particle size grows during combustion, we define an *expansion coefficient*:

$$K := -\frac{8 (\rho_g \mathcal{D}_O)_f \ln(1 - Y_{O,\infty})}{\rho_1}. \quad (35)$$

Consequently, Eq. (34) becomes

$$d_p^2 = d_0^2 + Kt. \quad (36)$$

Equation (36) resembles the size evolution of a shrinking droplet during vaporization (i.e., $d^2 = d_0^2 - \beta t$ with β the *evaporation coefficient* [1]). Substituting the final condition of combustion (i.e., $t = t_b$: $d_p = d_1$ and d_1 is the final particle diameter) into Eq. (34) gives the analytical solution for the burn time:

$$t_b = \frac{\rho_1 (d_0^2 - d_1^2)}{8 (\rho_g \mathcal{D}_O)_f \ln(1 - Y_{O,\infty})} = \frac{\rho_1 (1 - \epsilon^2) d_0^2}{8 (\rho_g \mathcal{D}_O)_f \ln(1 - Y_{O,\infty})}, \quad (37)$$

with $\epsilon := d_1/d_0$ defining the diameter expansion ratio. Equation (37) indicates a d_0^2 -dependence of the burn time in the diffusion-limited regime. Besides, using the time-dependent density and diameter of the particle, given in Eq. (29) and Eq. (36) respectively, the transient increase of the particle mass is determined as

$$m_p = \frac{\pi}{6} \left[\rho_1 (d_0^2 + Kt)^{3/2} + \rho_2 d_0^3 \right]. \quad (38)$$

Substituting Eq. (38) into Eq. (A.7) and normalize the result by the initial particle mass gives the fraction of remaining unburned metal in the particle during combustion:

$$\frac{m_m}{m_0} = (1 - s) \left[\frac{\rho_1}{\rho_m} \left(1 + \frac{K}{d_0^2} t \right)^{3/2} + \frac{\rho_2}{\rho_m} \right] + s. \quad (39)$$

2.3. Analytical solution for transient particle temperature

For some metals (e.g., Fe), a majority of the combustion process is in the liquid phase, where the specific heats of the metal and the oxide are close and independent of temperature [22]. Therefore, the specific heat of the particle does not change significantly during combustion. Assuming a constant specific heat of the particle, the governing equation of the particle temperature is expressed as

$$c_{p,p} \frac{d(m_p T_p)}{dt} = c_{p,p} m_p \frac{dT_p}{dt} + c_{p,p} T_p \frac{dm_p}{dt} = \dot{Q}_{\text{conv}} + \dot{Q}_{\text{chem}} + \dot{Q}_{\text{rad}}, \quad (40)$$

with $c_{p,p}$ being the specific heat of the particle, $m_p = \rho_p \pi d_p^3 / 6$ the particle mass, \dot{Q}_{conv} the convective heat transfer rate, \dot{Q}_{chem} the chemical heat release rate, and \dot{Q}_{rad} the radiative heat loss rate. Since only nonvolatile combustion is considered

in this work, the heat loss via evaporation is neglected. Although evaporation may become important when the particle temperature approaches the boiling point of the metal or the oxide, it is beyond the scope of strictly-defined nonvolatile combustion and makes the analytical solution seemingly impossible to complete. Consequently, the results derived here may be limited to scenarios where the maximum particle temperature is considerably below the boiling points. Combining Eqs. (16) and (28) gives the rate of particle mass change in the diffusion-limited combustion regime:

$$\frac{dm_p}{dt} = \dot{m}_O = \text{Sh}(\rho_g \mathcal{D}_O)_f \pi d_p Y_{O,\infty}, \quad (41)$$

Rewriting Eq. (26), the convective heat transfer rate reads

$$\dot{Q}_{\text{conv}} = \text{Nu} \lambda_f \pi d_p (T_{g,\infty} - T_p). \quad (42)$$

The chemical heat release rate is written as

$$\dot{Q}_{\text{chem}} = \dot{m}_{O_2} \phi \Delta h, \quad (43)$$

where ϕ is the stoichiometric fuel-to-oxygen mass ratio, and Δh is the combustion enthalpy per gram fuel. The radiative heat transfer rate is described by the Stefan-Boltzmann law:

$$\dot{Q}_{\text{rad}} = -\pi d_p^2 \varepsilon \sigma (T_p^4 - T_0^4), \quad (44)$$

where ε is the emissivity of the particle surface and σ is the Stefan-Boltzmann constant. Substituting Eqs. (41) to (44) into Eq. (40) and rearranging it yields:

$$\begin{aligned} c_{p,p} \frac{\rho_p d_p^2}{6} \frac{dT_p}{dt} &= \text{Nu} \lambda_f T_{g,\infty} + \text{Sh}(\rho_g \mathcal{D}_O)_f Y_{O,\infty} \phi \Delta h \\ &\quad - (\text{Nu} \lambda_f + \text{Sh}(\rho_g \mathcal{D}_O)_f Y_{O,\infty} c_{p,p}) T_p \\ &\quad - d_p \varepsilon \sigma (T_p^4 - T_0^4). \end{aligned} \quad (45)$$

With $\rho_p = \rho_1 + \rho_2 (d_0/d_p)^3$ (Eq. (29)) and $d_p^2 = d_0^2 + Kt$ (Eq. (36)), the following equation is obtained:

$$\rho_p d_p^2 = \rho_1 d_p^2 + \rho_2 \frac{d_0^3}{d_p} = \rho_1 (d_0^2 + Kt) + \rho_2 \frac{d_0^3}{\sqrt{d_0^2 + Kt}}. \quad (46)$$

In order to solve Eq. (45) analytically, Eq. (46) needs to be approximated. To this end, we consider the Taylor expansion at $t = 0$ for the second term on the right-hand side of Eq. (46), which expresses as

$$\frac{d_0^3}{\sqrt{d_0^2 + Kt}} = \frac{d_0^2}{\sqrt{1 + (K/d_0^2)t}} = \sum_{n=0}^{\infty} \left(\frac{K}{d_0^2} t \right)^n \frac{(2n-1)!!}{n!(-2)^n} d_0^2. \quad (47)$$

Recalling Eqs. (36), (A.10) and (A.12), one can find the following inequality valid for many metals with examples given in Table 1, where thermal expansion is neglected:

$$\left| \frac{K}{d_0^2} t \right| = \frac{d_p^2}{d_0^2} - 1 \leq \frac{d_1^2}{d_0^2} - 1 = \left(\frac{\rho_m \mathcal{M}_{\text{mo}}}{\rho_{\text{mo}} \mathcal{M}_m x} \right)^{2/3} - 1 < 1, \quad \forall t \in [0, t_b], \quad (48)$$

in which \mathcal{M}_m and \mathcal{M}_{mo} are the molar mass of the metal and the metal oxide, respectively, x is the numbers of metal atom in the chemical formula of the metal oxide, M_xO_y . Therefore, higher order terms in Eq. (48) become smaller. By neglecting $\mathcal{O}(t^2)$ ¹, Eq. (47) is approximated as

$$\frac{d_0^3}{\sqrt{d_0^2 + Kt}} \approx d_0^2 - \frac{K}{2}t, \quad \forall t \in [0, t_b]. \quad (49)$$

Then, Eq. (46) is also approximated as

$$\begin{aligned} \rho_p d_p^2 &\approx \rho_1 (d_0^2 + Kt) + \rho_2 \left(d_0^2 - \frac{K}{2}t \right) \\ &= (\rho_1 + \rho_2) d_0^2 + \left(\rho_1 - \frac{\rho_2}{2} \right) Kt \end{aligned} \quad (50)$$

The maximum truncation errors in Eqs. (49) and (50) introduced by the neglect of higher order terms in the Taylor series, Eq. (47), reach at t_b , which do not exceed 5% as provided in Table 1 for several sample metals. Substituting Eq. (50) into

¹It is possible to find a solution when the second order is included but the improvement is negligibly small and the expression is cumbersome. Therefore, we do not present it in the paper.

Eq. (45) and reagranging it yields

$$\begin{aligned} \left(1 + \frac{2\rho_1 - \rho_2}{2(\rho_1 + \rho_2)d_0^2}Kt\right) \frac{dT_p}{dt} &\approx 6 \frac{\text{Nu}\lambda_f T_{g,\infty} + \text{Sh}(\rho_g \mathfrak{D}_O)_f Y_{O,\infty} \phi \Delta h}{c_{p,p}(\rho_1 + \rho_2)d_0^2} \\ &- 6 \frac{\text{Nu}\lambda_f + \text{Sh}(\rho_g \mathfrak{D}_O)_f Y_{O,\infty} c_{p,p} T_p}{c_{p,p}(\rho_1 + \rho_2)d_0^2} \\ &- 6 \frac{d_p \varepsilon \sigma (T_p^4 - T_0^4)}{c_{p,p}(\rho_1 + \rho_2)d_0^2} \end{aligned} \quad (51)$$

By defining constant parameters as follows:

$$\mathfrak{B} := \frac{2\rho_1 - \rho_2}{2(\rho_1 + \rho_2)d_0^2}K, \quad (52)$$

$$\mathfrak{D} := 6 \frac{\text{Nu}\lambda_f T_{g,\infty} + \text{Sh}(\rho_g \mathfrak{D}_O)_f Y_{O,\infty} \phi \Delta h}{c_{p,p}(\rho_1 + \rho_2)d_0^2}, \quad (53)$$

$$\mathfrak{E} := 6 \frac{\text{Nu}\lambda_f + \text{Sh}(\rho_g \mathfrak{D}_O)_f Y_{O,\infty} c_{p,p}}{c_{p,p}(\rho_1 + \rho_2)d_0^2}, \quad (54)$$

and a non-linear function:

$$\mathbf{F}(T_p) := 6 \frac{d_p \varepsilon \sigma (T_p^4 - T_0^4)}{c_{p,p}(\rho_1 + \rho_2)d_0^2} \approx 6 \frac{\varepsilon \sigma (T_p^4 - T_0^4)}{c_{p,p}(\rho_1 + \rho_2)d_0} \quad (55)$$

in which the approximation is obtained by replacing d_p with d_0 . Alternatively, d_p can also be replaced by d_1 . The difference in the solved maximum particle temperatures that will be discussed in Section 3 is only around 1% between these two approximations, which can be regarded as negligible. The exact solution is bounded by those solved using these two approximations. Substituting Eqs. (52) to (55) into Eq. (51) simplifies it as

$$(1 + \mathfrak{B}t) \frac{dT_p}{dt} \approx \mathfrak{D} - \mathfrak{E}T_p - \mathbf{F}(T_p). \quad (56)$$

Rearranging Eq. (56) and integrating both sides yields

$$\int \frac{dT_p}{\mathfrak{D} - \mathfrak{E}T_p - \mathbf{F}(T_p)} \approx \int \frac{dt}{1 + \mathfrak{B}t} \quad (57)$$

To derive an explicit solution for $T_p(t)$ from Eq. (57), we first neglect radiation, i.e., $\mathbf{F}(T_p) = 0$. Then the general solution of Eq. (57) expresses as

$$T_p(t) \approx k_1(1 + \mathfrak{B}t)^{-\mathfrak{E}/\mathfrak{B}} + \frac{\mathfrak{D}}{\mathfrak{E}}, \quad (58)$$

with k_1 the constant of integration, which can be determined as

$$k_1 = T_{p,\text{ign}} - \frac{\mathfrak{D}}{\mathfrak{E}}, \quad (59)$$

using the initial condition:

$$t = 0 : T_p(0) = T_{p,\text{ign}}. \quad (60)$$

Finally, the explicit solution of Eq. (51) reads

$$T_p(t) \approx \left(T_{p,\text{ign}} - \frac{\mathfrak{D}}{\mathfrak{E}} \right) (1 + \mathfrak{B}t)^{-\mathfrak{E}/\mathfrak{B}} + \frac{\mathfrak{D}}{\mathfrak{E}}. \quad (61)$$

When radiation is considered, an explicit solution cannot be found but T_p can be expressed implicitly as

$$t \approx \frac{1}{\mathfrak{B}} \left[\exp \left(\int_{T_{p,\text{ign}}}^{T_p(t)} \frac{\mathfrak{B}dz}{\mathfrak{D} - \mathfrak{E}z - \mathbf{F}(z)} \right) - 1 \right]. \quad (62)$$

The integral in Eq. (62) can be solved analytically using partial fraction decomposition, yielding

$$\int_{T_{p,\text{ign}}}^{T_p(t)} \frac{\mathfrak{B}dz}{\mathfrak{D} - \mathfrak{E}z - \mathbf{F}(z)} = \mathfrak{B} \sum_{\omega_i} \frac{\ln(T_{p,\text{ign}} - \omega_i) - \ln(T_p - \omega_i)}{4\mathfrak{F}\omega_i + \mathfrak{E}}, \quad (63)$$

where ω_i is the complex roots of the quartic equation $\mathfrak{D} - \mathfrak{E}\omega - \mathbf{F}(\omega) = 0$ and \mathfrak{F} is a constant defined as

$$\mathfrak{F} := 6 \frac{\varepsilon\sigma}{c_{p,p}(\rho_1 + \rho_2)d_0} \quad (64)$$

Table 1: Values of $d_1^2/d_0^2 - 1$ for selected metals and oxides, along with the corresponding truncation errors (TE) induced by the linear approximation in Eqs. (49) and (50), respectively.

Metal	Oxide	$d_1^2/d_0^2 - 1$	TE in Eq. (49)	TE in Eq. (50)
Al	Al ₂ O ₃	0.19	-1.3%	1.3%
Si	SiO ₂	0.52	-8.8%	1.2%
Fe	FeO	0.46	-7.0%	-3.4%

2.4. Coupling of solutions and computational procedure

The analytical solutions for particle burn time and temperature evolution have been derived separately. However they are conjugated via the mass diffusivity of the oxygen at the film layer, $(\rho_g \mathcal{D}_O)_f$. The mass diffusivity is unknown *a priori* since it is evaluated at the film layer temperature, T_f , whose determination needs the particle temperature as shown in Eq. (7). Since the particle temperature is transient, so is the film layer temperature.

Considering the fact that $(\rho_g \mathcal{D}_O)_f \propto T_f^{0.7}$ for diatomic gases, which is close to be a linear correlation, the following approximate relation is obtained:

$$(\rho_g \mathcal{D}_O)_f \approx (1 - A_f) T_p + A_f T_{g,\infty} \quad (65)$$

This approximation implies that, on the one hand, the variation of $(\rho_g \mathcal{D}_O)_f$ during particle combustion is not significant owing to a constant far-field gas temperature. On the other hand, due to the linear proportionality, an averaged $(\rho_g \mathcal{D}_O)_f$ could be evaluated at a time-averaged film layer temperature:

$$\langle T_f \rangle = (1 - A_f) \langle T_p \rangle + A_f T_{g,\infty} \quad (66a)$$

with $\langle T_p \rangle$ the time-averaged particle temperature:

$$\langle T_p \rangle = \frac{1}{t_b} \int_0^{t_b} T_p(t) dt \quad (66b)$$

To obtain quantitative results, the time-average temperature and gas composition at the film layer are determined iteratively using the procedure illustrated in Fig. 2. The thermal physical and transport properties of the gaseous mixture and species at the film layer are evaluated using Cantera [23].

3. Application to iron particle combustion

In this section, the theory developed above is applied to analyze the burning properties of micron-sized iron particles, which serves as a typical example of

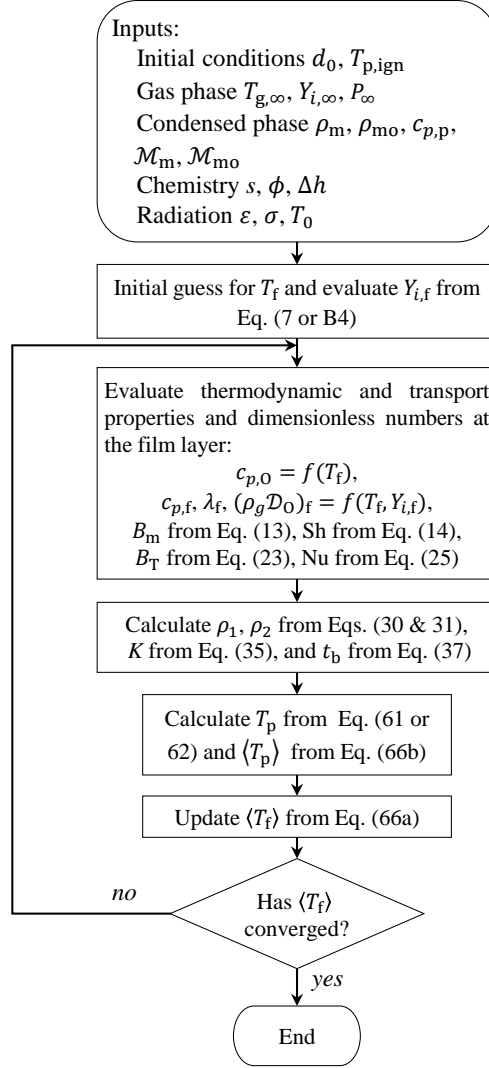


Figure 2: Calculation procedure for obtaining the quantitative solution of the burn time and temperature history .

non-volatile, heterogeneous combustion at low to moderate oxygen concentrations. This choice is justified by the much higher boiling points of iron and iron oxides (> 3000 K at 1 atm) compared to the peak temperature of the burning particles in air at room temperature (~ 2500 K [13]). Additionally, systematic experiments providing quantitative data have been conducted, offering an opportunity to validate

the theory.

3.1. Iron-oriented assumptions and parameters

The basic assumptions, which were adopted to reasonably simplify the practical problem, leading to the successful derivation of the theory, such as constant thermophysical properties and homogeneous distributions of temperature inside the particle, remain unchanged. The main assumptions related to iron particle combustion are three-fold. First, the ignition temperature is assumed to be 1100 K, as suggested by the calculations using a state-of-the-art model [24]. Second, the oxidation reaction is assumed to be $\text{Fe} + \text{O}_2 \rightarrow \text{FeO}$, and combustion enthalpy per gram iron is determined by the NASA thermodynamic database. Third, the reaction stops upon completely conversion to FeO, and further oxidation is neglected. The physical parameters used for performing the quantitative analysis of iron particle combustion are listed in Table 2.

Table 2: Physical parameters for iron particle combustion.

Parameter	Value	Unit
$c_{p,p}$	0.94	$\text{J} \cdot \text{K}^{-1} \cdot \text{g}^{-1}$
ρ_{Fe}	7.874	$\text{g} \cdot \text{cm}^{-3}$
ρ_{FeO}	5.740	$\text{g} \cdot \text{cm}^{-3}$
ϕ	3.5	-
Δh	4875	$\text{J} \cdot \text{g}^{-1}$

3.2. Theoretical results and discussion

In this section, sample results on the combustion characteristics of iron particles under different boundary and initial conditions will be presented. The mechanisms underling the theoretical results are explained.

3.2.1. Effects of particle size and surface radiation

Figure 3 illustrates the quantitative solutions for the temperature and the fraction of unburnt iron of a 40 μm and a 60 μm iron particles during combustion in the 21% O_2 /79% N_2 at 300 K, both with and without considering radiation. When the radiative heat loss is neglected, the two particles reach the same peak temperature of 2578 K at approximately 14 ms and 32 ms, respectively. By the same time, iron has burnt out, as indicated by the disappearance of unburnt iron mass in Fig. 3(a). The independence of the particle peak temperature on the diameter arises because

d_0 cancels out from the analytical solution for the particle peak temperature, as derived in Eq. (67). This solution is obtained by substituting the particle burn time solution, Eq. (37), into the radiation-excluded expression of particle temperature history, Eq. (58).

$$T_{p,\max} \approx \left(T_{p,\text{ign}} - \frac{\mathfrak{D}}{\mathfrak{E}} \right) \left(1 + \frac{(2\rho_1 - \rho_2)(1 - \epsilon^2)}{2(\rho_1 + \rho_2)} \right)^{-\mathfrak{E}/\mathfrak{B}} + \frac{\mathfrak{D}}{\mathfrak{E}}. \quad (67)$$

As time continues to elapse, the particle temperature still increases until reaching a plateau, corresponding to the steady-state solution for the particle temperature. This plateau represents the time-independent term, $\frac{\mathfrak{D}}{\mathfrak{E}}$, in Eq. (58). The steady-state solution is achieved when the rates of the conductive heat loss and the chemical heat release are balanced. However, this solution is nonphysical because it yields a negative value for the unburnt mass of iron. When radiation is considered, the dependence of the particle peak temperature on the particle diameter emerges, indicating that the larger particle has a lower peak temperature. The maximum temperatures of the small and large particles are 2456 K and 2402 K, about 60 K and 90 K lower than their non-radiative counterparts, respectively. Additionally, Fig. 3 shows that the effect of radiative heat loss on particle burn times is negligible. The overall temporal evolution of the particle temperature, including both the physical and nonphysical solutions, clearly depicts that the maximum particle temperature is constrained by the burnout of fuel rather than heat losses.

The time history of the particle temperature and the fraction of unburnt iron shown in Fig. 3 are re-plotted versus the time coordinated normalized by the initial particle diameter squared (i.e., t/d_0^2) in Fig. 4. Curves for different particle diameters overlap when radiation is neglected. As the initial particle diameter, d_0 , drops out in $\mathfrak{D}/\mathfrak{E}$ and $\mathfrak{E}/\mathfrak{B}$, the effect of the initial particle diameter on the particle temperature, described by Eq. (58), appears only in the term:

$$\mathfrak{B}t = \frac{2\rho_1 - \rho_2}{2(\rho_1 + \rho_2)} K \cdot \frac{t}{d_0^2}. \quad (68)$$

As the first factor of the right hand side of Eq. (68) is independent of d_0 , the particle temperature history scales with $1/d_0^2$ when radiation is neglected. This scaling behavior is also valid for the fraction of unburnt iron, as described by Eq. (39). Even when accounting for radiation, the curves for 40 and 60 μm coincide very well. For particle peak temperatures below approximately ~ 2500 K, radiation appears to have a weak impact on controlling the temperature evolution of burning iron particles, particularly for particles with relatively small diameters

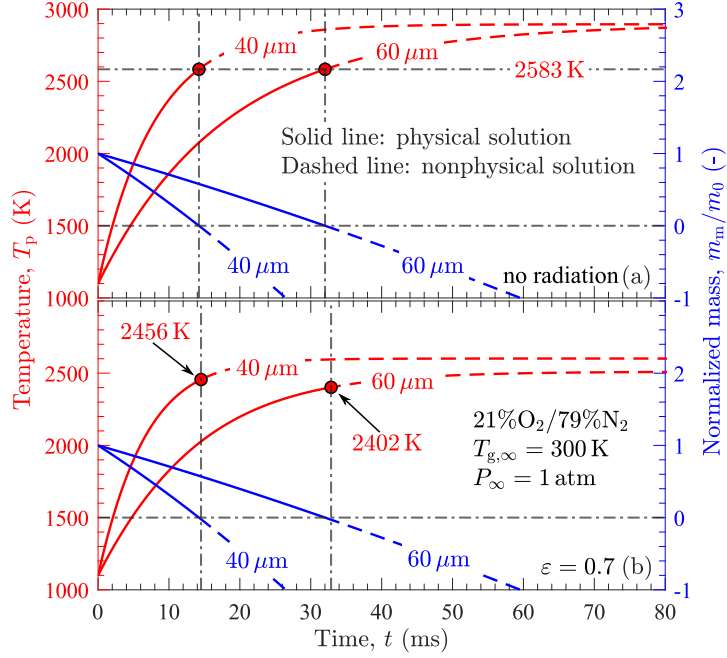


Figure 3: Theoretical temperature history and fraction of unburned iron during the combustion of a $40\ \mu\text{m}$ and a $60\ \mu\text{m}$ iron particles burning in the $21\%\text{O}_2/79\%\text{N}_2$ mixture at $T_{g,\infty} = 300\ \text{K}$ and $P_\infty = 1\ \text{atm}$, (a) without radiation and (b) with radiation ($\varepsilon = 0.7$).

(e.g., $< 100\ \mu\text{m}$). This scaling is consistent with the expanding d^2 -law derived in Eq. (36).

3.2.2. Effects of gas-phase pressure and temperature

Figure 5 depicts the burn time and temperature history of a $50\ \mu\text{m}$ iron particle under varying gas-phase pressure, P_∞ , and temperature, T_∞ . Increasing the ambient pressure from $1\ \text{atm}$ to $10\ \text{atm}$ exhibits no discernible impact on the diffusion-limited combustion process of the particle. The independence of particle burn time from ambient pressure is attributed to the negligible influence of pressure on the mass diffusivity of the oxygen at the film layer, denoted as $(\rho_g \mathcal{D}_O)_f$, a critical factor controlling the duration of particle combustion in the diffusion-limited regime. The gas density, ρ_g , scales linearly with pressure and the binary diffusion coefficient of oxygen, \mathcal{D}_O , is inversely proportional to pressure according to Chapman-Enskog theory [25]. Additionally, the thermal conductivity of ideal gases remains independent of pressure, except at extremely low pressures where the mean free path approaches or surpasses the dimensions of fuel particles

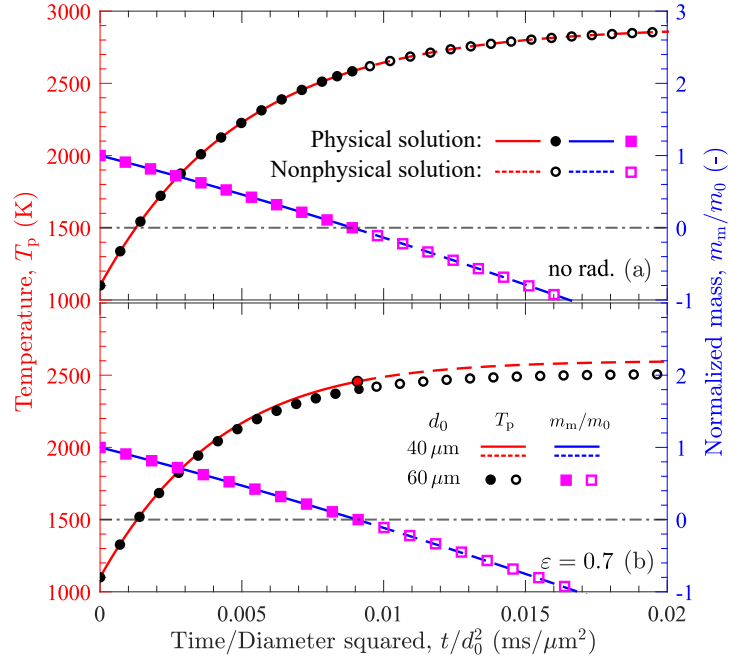


Figure 4: Scaled temperature history and fraction of unburned iron during the combustion of a 40 μm and a 60 μm iron particles burning at the room condition: 21% O_2 /79% N_2 , $T_{g,\infty} = 300\text{ K}$, and $P_\infty = 1\text{ atm}$, (a) without radiation and (b) with radiation ($\varepsilon = 0.7$).

(Knudsen number $\text{Kn} \ll 1$). Consequently, the governing equation for particle temperature (Eq. (51)) and its solutions (Eqs. (61) and (62)), depicting the time history of the particle temperature, are unaffected by ambient gas pressure.

In contrast to pressure, the burn time of the particle shortens with increasing the gas-phase temperature, ending at a higher maximum temperature. Figure 6(a) summarizes the peak particle temperature, $T_{p,\text{max}}$, and burn time normalized by the initial particle diameter squared, t_b/d_0^2 , as a function of the gas-phase temperature for 10 and 100 μm iron particles burning in the 14% O_2 /86% N_2 mixture. The calculation is conducted for particle peak temperatures below 2500 K, ensuring negligible evaporation. As shown in Figure 6(a), the peak temperature shows an almost linear correlation with the gas-phase temperature. Given that the role of radiation is significantly weaker in determining the maximum particle temperature compared to convection, the linear dependence of the particle peak temperature on the far-field gas temperature can be derived by rearranging Eq. (67), yielding

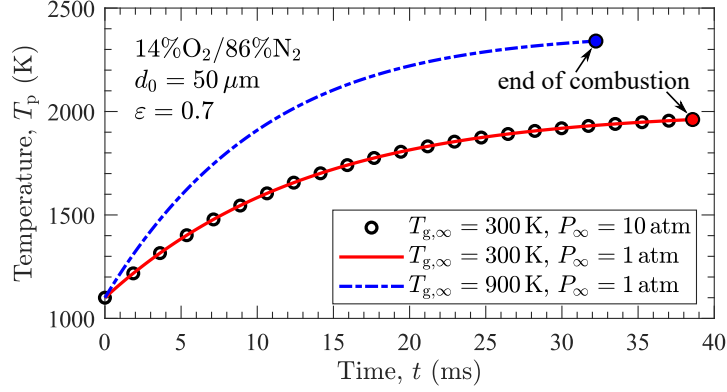


Figure 5: Time histories of temperature for a 50 μm particle when burning at different oxygen mole fractions and ambient pressures. The oxygen mole fraction of 14% is used to limit the maximum particle temperature below 2500 K at the ambient temperature of 900 K.

$$\begin{aligned}
T_{p,\max} \approx & (1 - \mathfrak{G}) \frac{\text{NuLe}_O c_{p,f}}{\text{NuLe}_O c_{p,f} + \text{Sh}Y_{O,\infty} c_{p,p}} T_{g,\infty} \\
& + (1 - \mathfrak{G}) \frac{Y_{O,\infty} \phi \Delta h}{\text{NuLe}_O c_{p,f} + \text{Sh}Y_{O,\infty} c_{p,p}} \\
& + T_{p,\text{ign}} \mathfrak{G},
\end{aligned} \tag{69a}$$

with the $T_{g,\infty}$ -independent constant \mathfrak{G} defined as

$$\mathfrak{G} := \left(1 + \frac{(2\rho_1 - \rho_2)(1 - \epsilon^2)}{2(\rho_1 + \rho_2)} \right)^{\frac{3}{4}} \frac{\text{NuLe}_O c_{p,f} + \text{Sh}Y_{O,\infty} c_{p,p}}{(2 - \rho_2/\rho_1) \ln(1 - Y_{O,\infty})}, \tag{69b}$$

where Le_O and $c_{p,g}$ are the Lewis number of the oxygen and the specific heat of the gaseous mixture evaluated at the film layer, respectively. In Eq. (69), all the other parameters are independent on the far-field gas temperature, $T_{g,\infty}$, and thus the linearity between $T_{p,\max}$ and $T_{g,\infty}$ is determined by the first term on the right hand side of the equation.

In Fig. 6(b), it is observed that as the far-field gas temperature increases, the particle burn time decreases in proportion to $T_f^{-0.7}$. This behavior is attributed to the fact that the mass diffusivity of the oxygen at the film layer is directly proportional to $T_f^{0.7}$, which increases with the rise in ambient gas temperature. Additionally, the larger particle exhibits a larger value of t_b/d_0^2 at the same gas temperature. This

can be attributed to increased heat loss through surface radiation. The heightened surface radiation leads to a reduction in the time-averaged particle temperature and, consequently, the time-averaged film-layer temperature, $\langle T_f \rangle$. This reduction in $\langle T_f \rangle$ contributes to a decrease in the mass diffusivity of the oxygen, resulting in larger values of t_b/d_0^2 .

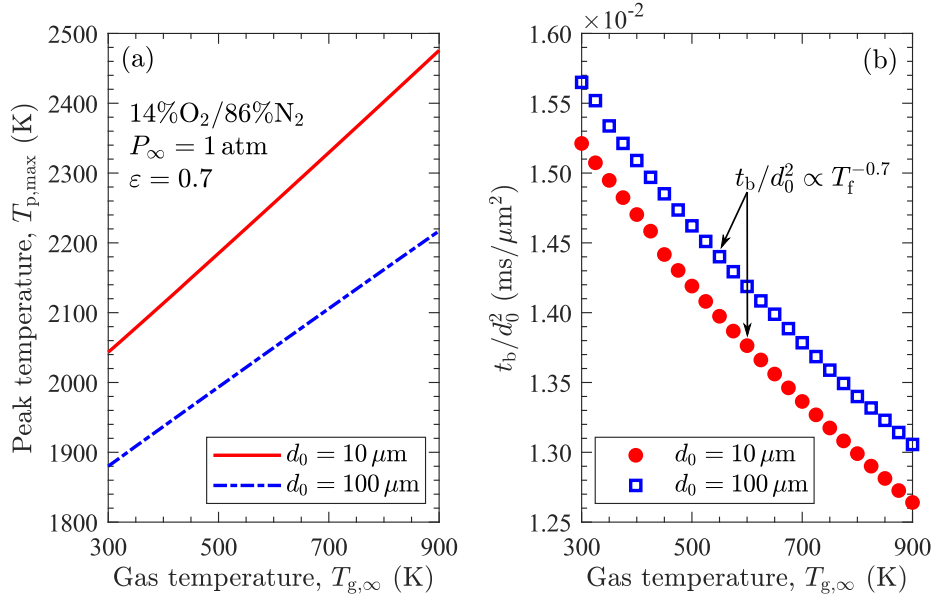


Figure 6: Particle peak temperature (a) and burn time scale with diameter squared (b) as a function of the far-field gas temperature.

3.2.3. Effect of initial particle temperature

Laser heating is a commonly employed experimental technique for initiating combustion in metal particles. Despite the advantages of being able to flexibly adjust the gas composition and temperature in laser-ignition experiments, there is a tendency for the particle to rapidly reach a high-temperature state in the diffusion regime without undergoing the typical ignition process. Since oxidation during laser heating is considered negligible, the resulting laser-driven high-temperature state can be treated as an initial particle temperature for theoretical analysis. This section examines the impact of the initial particle temperature on the combustion characteristics of iron particles.

Figure 7 shows the calculated time histories for different initial temperature of a $50 \mu\text{m}$ iron particle burning in a mixture of 21% O_2 /79% N_2 at 300 K and

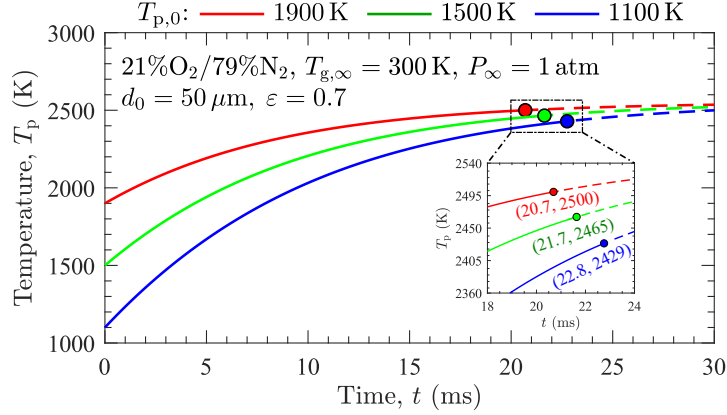


Figure 7: Time histories of a 50 μm iron particle with three different initial temperature, burning in the mixture of 21% O_2 /79% N_2 at $T_{g,\infty} = 300$ K, and $P_\infty = 1$ atm.

atmospherical pressure. Despite a temperature difference of 400 K between neighboring cases at the onset of combustion, the maximum particle temperatures at burnout are very close, with a difference of about 35 K. This weak effect of the initial temperature on the maximum particle temperature is attributed to the combustion progress closely approaching a steady state, where the initial condition has been largely relaxed. Moreover, the significant elevations of the initial particle temperature only induce very minor reductions (i.e., $< 10\%$) in the particle burn time. In the diffusion-limited regime, the insensitivity of the burn time to the initial particle temperature is due to the controlling parameter of particle burn time being the mass diffusivity of the oxygen $\rho_g \mathcal{D}_\text{O}$, evaluated using a time-averaged film layer temperature $\langle T_f \rangle$. According to Eq. (66), the role of the initial particle temperature in determining $\rho_g \mathcal{D}_\text{O}$ is significantly weakened by the two-fold averaging operations. For example, the calculated $\langle T_f \rangle$ in the cases of $T_{p,0} = 1100$ K and 1900 K shown in Fig. 7 are 1423 K and 1638 K, respectively. This means that an 73% variation in $T_{p,0}$ causes only a 15% change in $\langle T_f \rangle$. Since $\rho_g \mathcal{D}_\text{O} \propto \langle T_f \rangle^{0.7}$, the difference in the mass diffusivity of the oxygen further reduces to 9.7%, which finally determines the discrepancies between the particle burn times. The weak coupling between the burn time and temperature of the particle is a key feature of heterogeneous combustion in the diffusion-limited regime.

3.3. Comparison with experiments

To validate the predictive capability of the theory, the theoretical burn times and temperatures of micron-sized iron particles are compared with a series of

measurements reported in Refs. [3, 4, 13]. These measurements were conducted for isolated iron particles burning in O_2/N_2 mixtures at room temperature. As the particle temperature right after laser ignition could not be directly measured for most cases in the experiments [3, 13], an initial partial temperature of 1500 K is assumed, identical to that used in Ref. [9].

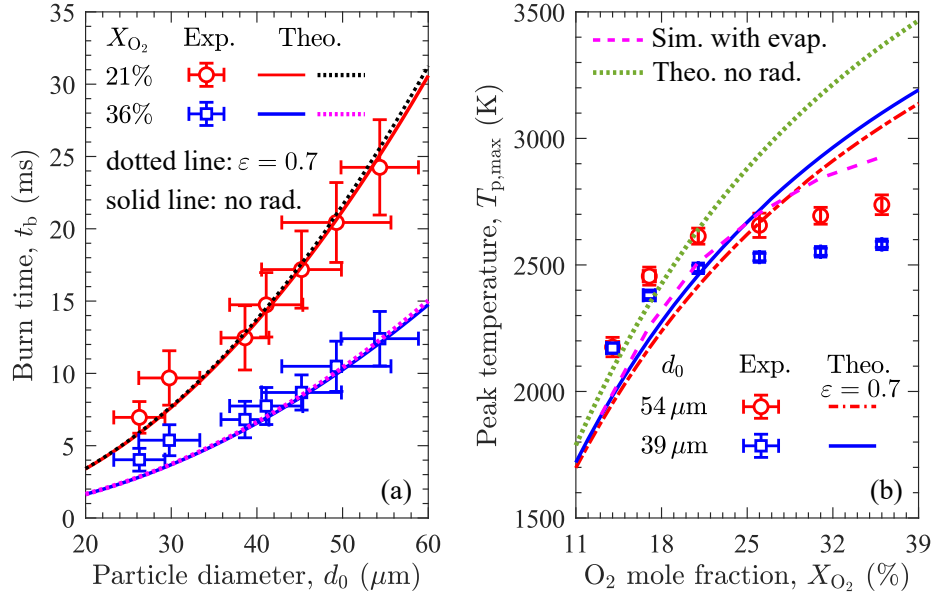


Figure 8: (a) Comparison between experimental and theoretical burn times of iron particles with various initial diameters. (b) Experimental, theoretical, and numerical particle peak temperature as a function of oxygen molar fractions. The experimental results are obtained for $39 \pm 2.8 \mu\text{m}$ and $54 \pm 4.5 \mu\text{m}$ particle size distributions. The theoretical results are calculated for the arithmetic mean diameters of $39 \mu\text{m}$ and $54 \mu\text{m}$, and the simulation results are for a $50 \mu\text{m}$ particle, adopted from Ref. [9].

Figure 8(a) reveals a comparison between the theoretical and experimental burn times of laser-ignited iron particles within the size range of 25–55 μm . The calculated burn times, based on the current theoretical model, exhibit almost perfect agreement with the measurements for initial particle diameters larger than 38 μm . Whereas for smaller particles, the theory slightly underestimates the burn time. This high level of agreement validates the quantitative accuracy of the current theoretical model in predicting particle burn times, not only at normal but also at elevated oxygen levels. Additionally, Fig. 8(b) compares the particle peak temperatures predicted by the theory with those approximately measured using a spectrometer [13]. In the experiment, the arithmetic mean diameters of the adopted

particle size distributions are 39 μm and 54 μm , respectively. For the theoretical calculation, the mean diameters are used. The results show that at oxygen mole fractions below approximately 26%, the theory reasonably captures the maximum particle temperature, although the measurements slightly surpass the calculations that include radiation. This discrepancy is likely attributed to the overestimation of the experimental approach, as the maximum particle temperatures are deduced from the measured gray-body emission spectra. As explained in Ref. [3], these spectra are prone to be dominated by the emissions of relatively hot particles appearing within the time period of data acquisition due to the strong dependence of thermal radiation on temperature. The maximum particle temperatures calculated without considering radiation are marginally higher than their radiation-included counterparts, especially at relatively low oxygen mole fractions. However, this discrepancy becomes more significant with increasing oxygen levels because the particle peak temperature rises, making radiative heat loss more prominent. Furthermore, the current theoretical results closely resemble particle-resolved direct numerical simulations for a 50 μm particle [9], which also incorporates the surface evaporation of liquid iron and oxide. When the mole fraction of oxygen exceeds 26%, both the numerical simulation and the present theory remarkably overpredict the particle peak temperature. As stated previously, evaporation is neglected in the theory, leading to the overprediction of the particle temperature at relatively high oxygen levels. In addition, this overestimation can also be attributed to the transition of the rate-limiting mechanism from external diffusion to either surface chemisorption [12] or internal diffusion of ions across the liquid oxide layer [10], which are neither considered in the theory nor the numerical simulation of Thijs et. al [9]. Given the excellent agreement between the measured burn time and the calculation based on the assumption of the external-diffusion-limited combustion regime, it is plausible that the other two potential rate-limiting mechanisms may only come into play for a brief period near the end of the liquid-phase combustion of iron particles, specifically in proximity to the particle peak temperature. For the majority of the iron particle combustion process, it is likely that external diffusion of the oxygen predominantly dictates the dynamics, making the inner structure of the particle less influential for predicting burn time.

Finally, the weak coupling between burn time and particle temperature suggests that while burn time is a necessary parameter, it alone is not sufficient to validate particle combustion modes. Time-resolved particle temperature emerges as a crucial experimental information for validating theoretical and numerical models of particle combustion. Figure 9 shows a comparison between the time histories calculated using the current theory and those measured using two-color pyrometry

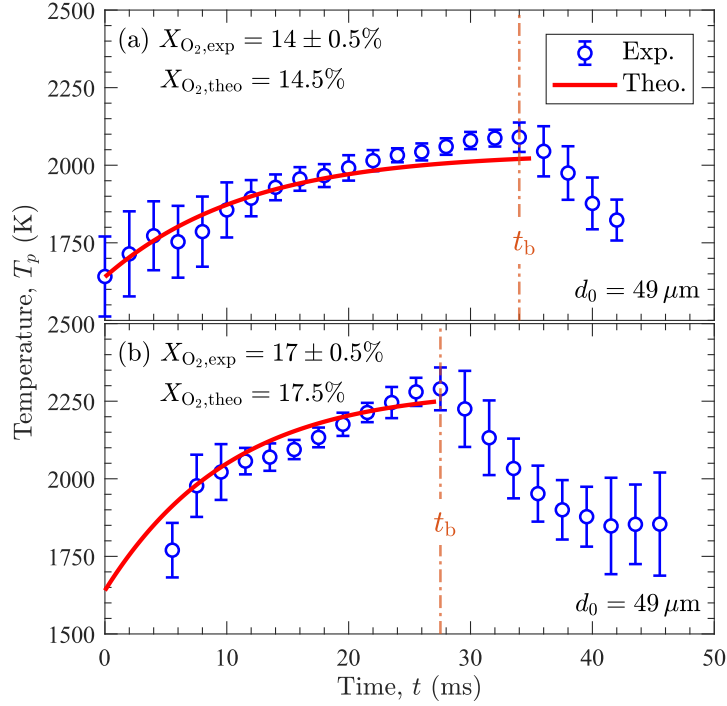


Figure 9: Theoretical and experimental temperature histories of $49\ \mu\text{m}$ iron particles burning at $14 \pm 0.5\%$ and $17 \pm 0.5\%$ oxygen mole fractions, respectively. The solid curves represent theoretically calculated results for $49\ \mu\text{m}$ particles without radiative heat loss. The symbols denote experimentally obtained mean results with standard deviation for $49 \pm 5\ \mu\text{m}$ particles, as reported in Ref. [4]. For the sake of clarity, the experimental data are plotted in every 2 ms.

[4]. For the theoretical calculation, the initial temperature and mean particle size are taken from the experiment. It worth noting that the initial particle temperature was only directly measured at the relatively low oxygen mole fraction of 14%. At the oxygen mole fraction of 17%, the same initial particle temperature is assumed in the theory because the particles were heated up with an identical laser power of 40 W. As illustrated in Fig. 9(a), the time history of the theoretical particle temperature generally aligns well with the measurement. Approaching the maximum particle temperature, the theory slightly underpredicts the measurement. The comparison ends at the peak temperature, since further oxidation beyond stoichiometric FeO during subsequent reactive cooling is not considered. As at higher oxygen mole fraction of $17 \pm 0.5\%$, where the particle temperature right after ignition was not measured, the initial event of the measured temperature trajectory cannot represent the start of the combustion process. To establish an absolute

time coordinate for the comparison with the theory, in Fig. 9(b) the measured temperature profile is shifted to match with the burn time extrapolated from a fitted correlation between burn time and the initial particle diameter [19]. The good agreement confirms that the current theoretical model accurately predicts the time-dependent temperature of burning iron particles, providing a robust validation for scenarios where the particle peak time is much lower than the boiling point of iron, leading to a negligible impact of evaporation.

4. Conclusions and outlook

This work introduces a quantitative analytical theory for the diffusion-limited combustion of nonvolatile (metal) particles. Analytical solutions for the burn time and time-dependent particle temperature are derived from the conservation equations. A simple and effective approach is proposed to couple the solutions, which demonstrates a remarkable predictive capability without relying on numerical or experimental inputs. The application of the model to analyze iron particle combustion provides valuable insights into the underlying processes.

First of all, the peak temperature of the particle is constrained by the burnout of iron rather than the balance between the heat generation and heat loss of the particle. When radiation is excluded, the time-dependent parameters of the particle, including temperature, diameter, and the fraction of unburnt metal, follows a scaling of $1/d_0^2$ along the time coordinate. Taking the surface radiation into account do not change the scaling significantly, whereas it introduces a negative size-dependence of the particle temperature.

Furthermore, the gas-phase pressure, if not very low, plays no role in the diffusion-limited combustion process of nonvolatile particles when the evaporation is negligible. In contrast, increasing the far-field gas temperature accelerates the combustion process, which results in an elevated particle peak temperature following a nearly linear trend with respect to the gas temperature. As the mass diffusivity of the oxygen is insensitive to the initial particle temperature, the burn time in the diffusion limited regime only slightly changes even for large variations of the initial particle temperature. By the time when the particle peak temperature is reached, the initial temperature has been largely relaxed. Consequently, the peak temperature is weakly influence by the initial condition.

Finally, the theoretical predictions for the burn time and temperature of isolated iron particle are compared with their experimental counterparts. The quantitatively accurate alignment between the theoretical and experimental results validates the model within the scope of its applicable assumptions. The presented theory not

only stands as a valuable tool for predicting combustion characteristics of iron particles but also serves as a foundation for future studies exploring the intricacies of nonvolatile particle combustion in diverse scenarios.

Declaration of competing interest

The authors declare that they have no known competing financial interests or personal relationships that could have appeared to influence the work reported in this paper.

Acknowledgments

This work is funded by the Hessian Ministry of Higher Education, Research, Science and the Arts under the cluster project Clean Circles.

References

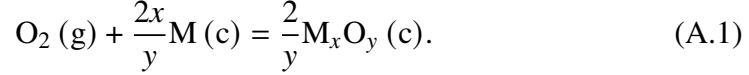
- [1] I. Glassman, R. A. Yetter, N. G. Glumac, *Combustion*, Academic press, 5th Edition, 2015.
- [2] A. Wright, S. Goroshin, A. Higgins, *Combustion time and ignition temperature of iron particles in different oxidizing environments* (2015).
- [3] D. Ning, Y. Shoshin, J. A. van Oijen, G. Finotello, L. De Goey, *Burn time and combustion regime of laser-ignited single iron particle*, *Combust. Flame* 230 (2021) 111424.
- [4] D. Ning, Y. Shoshin, J. van Oijen, G. Finotello, P. de Goey, *Size evolution during laser-ignited single iron particle combustion*, *Proc. Combust. Inst.* 39 (2023) 3561–3571.
- [5] S. Li, J. Huang, W. Weng, Y. Qian, X. Lu, M. Aldén, Z. Li, *Ignition and combustion behavior of single micron-sized iron particle in hot gas flow*, *Combust. Flame* 241 (2022) 112099.
- [6] D. Ning, T. Li, J. Mich, A. Scholtissek, B. Böhm, A. Dreizler, *Multi-stage oxidation of iron particles in a flame-generated hot laminar flow*, *Combust. Flame* 256 (2023) 112950.

- [7] P. Tóth, Y. Ögren, A. Sepman, P. Gren, H. Wiinikka, Combustion behavior of pulverized sponge iron as a recyclable electrofuel, *Powder Technol.* 373 (2020) 210–219.
- [8] A. Panahi, D. Chang, M. Schiemann, A. Fujinawa, X. Mi, J. M. Bergthorson, Y. A. Levendis, Combustion behavior of single iron particles-part i: An experimental study in a drop-tube furnace under high heating rates and high temperatures, *Appl. Energy Combust. Sci.* 13 (2023) 100097.
- [9] L. Thijs, C. van Gool, W. Ramaekers, J. A. van Oijen, L. de Goey, Resolved simulations of single iron particle combustion and the release of nano-particles, *Proc. Combust. Inst.* 39 (2023) 3551–3559.
- [10] A. Fujinawa, L. C. Thijs, J. Jean-Philippe, A. Panahi, D. Chang, M. Schiemann, Y. A. Levendis, J. M. Bergthorson, X. Mi, Combustion behavior of single iron particles, part ii: A theoretical analysis based on a zero-dimensional model, *Appl. Energy Combust. Sci.* 14 (2023) 100145.
- [11] S. Xu, Y. Qiu, L. Xu, J. Huang, S. Li, E. J. Nilsson, Z. Li, W. Cai, M. Aldén, X.-S. Bai, Phase change and combustion of iron particles in premixed $ch_4/o_2/n_2$ flames, *Combust. Flame* 259 (2024) 113171.
- [12] L. C. Thijs, E. M. Kritikos, A. Giusti, G. Ramaekers, J. A. van Oijen, P. de Goey, X. Mi, On the surface chemisorption of oxidizing fine iron particles: Insights gained from molecular dynamics simulations, *Combust. Flame* 254 (2023) 112871.
- [13] D. Ning, Y. Shoshin, M. van Stiphout, J. van Oijen, G. Finotello, P. de Goey, Temperature and phase transitions of laser-ignited single iron particle, *Combust. Flame* 236 (2022) 111801.
- [14] D. Ning, Y. Shoshin, J. A. van Oijen, G. Finotello, L. P. de Goey, Critical temperature for nanoparticle cloud formation during combustion of single micron-sized iron particle, *Combust. Flame* 244 (2022) 112296.
- [15] M. Bidabadi, M. Mafi, Analytical modeling of combustion of a single iron particle burning in the gaseous oxidizing medium, *Proc. Inst. Mech. Eng. C-J. Mec.* 227 (2013) 1006–1021.

- [16] P. Maghsoudi, M. Bidabadi, S. A. H. Madani, A. Afzalabadi, Analytical investigation of temperature of a single micron sized iron particle during combustion, *J. Cent. South Univ* 27 (2020) 951–962.
- [17] M. Bidabadi, M. Mafi, Time variation of combustion temperature and burning time of a single iron particle, *Int. J. Therm. Sci.* 65 (2013) 136–147.
- [18] T. Hazenberg, An eulerian-lagrangian approach for simulating heterogeneous combustion of metal fuels (2019).
- [19] D. Ning, T. Hazenberg, Y. Shoshin, J. van Oijen, G. Finotello, L. de Goey, Experimental and theoretical study of single iron particle combustion under low-oxygen dilution conditions, *Fuel* 357 (2024) 129718.
- [20] G. Hubbard, V. Denny, A. Mills, Droplet evaporation: effects of transients and variable properties, *Int. J. Heat Mass Tran.* 18 (1975) 1003–1008.
- [21] D. Spalding, A standard formulation of the steady convective mass transfer problem, *Int. J. Heat Mass Tran.* 1 (1960) 192–207.
- [22] M. W. Chase, N. I. S. O. (US), NIST-JANAF thermochemical tables, volume 9, American Chemical Society Washington, DC, 1998.
- [23] D. G. Goodwin, H. K. Moffat, I. Schoegl, R. L. Speth, B. W. Weber, Cantera: An object-oriented software toolkit for chemical kinetics, thermodynamics, and transport processes, 2022. Version 2.6.0.
- [24] X. Mi, A. Fujinawa, J. M. Bergthorson, A quantitative analysis of the ignition characteristics of fine iron particles, *Combust. Flame* 240 (2022) 112011.
- [25] J. O. Hirschfelder, C. F. Curtiss, R. B. Bird, et al., *Molecular theory of gases and liquids*, Wiley New York, 1954.

Appendix A. Size-dependent particle density

An universal expression of the oxidation reaction of metal with oxygen reads



Therefore, a stoichiometric oxide-to-oxygen mass ratio can be defined as

$$s := \frac{2 \mathcal{M}_{\text{mo}}}{y \mathcal{M}_{\text{O}_2}}, \quad (\text{A.2})$$

with \mathcal{M}_{mo} and \mathcal{M}_{O_2} the molar mass of the metal oxide ($\text{M}_x \text{O}_y$) and that of O_2 . The mass of the particle encompassing those of total oxygen and metal elements reads

$$m_{\text{p}} = m_{\text{M}} + m_{\text{O}}, \quad (\text{A.3})$$

where subscripts, M and O, denote the metal and oxygen elements, respectively. The total mass of metal elements is essentially the initial mass of the metal particle:

$$m_{\text{M}} = m_0 = \frac{\pi}{6} \rho_{\text{m}} d_0^3, \quad (\text{A.4})$$

with d_0 the initial particle diameter and ρ_{m} the density of the metal. Because of the conservation of O elements, the total mass of O elements in the particle equals that of consumed O_2 :

$$m_{\text{O}} = m_{\text{O}_2}. \quad (\text{A.5})$$

According to Eqs. (A.2), (A.3) and (A.5), the mass of metal oxide is:

$$m_{\text{mo}} = s m_{\text{O}_2} = s m_{\text{O}} = s(m_{\text{p}} - m_{\text{M}}) = s(m_{\text{p}} - m_0), \quad (\text{A.6})$$

The remaining mass of the metal is

$$m_{\text{m}} = m_{\text{p}} - m_{\text{mo}} = (1 - s)m_{\text{p}} + s m_0. \quad (\text{A.7})$$

Assuming the volumetric shrinkage due to mixing between liquid metal and liquid metal oxide (if they are miscible) is negligible, the volume of the particle is

$$\frac{m_{\text{p}}}{\rho_{\text{p}}} = V_{\text{p}} = V_{\text{mo}} + V_{\text{m}} = \frac{m_{\text{mo}}}{\rho_{\text{mo}}} + \frac{m_{\text{m}}}{\rho_{\text{m}}}. \quad (\text{A.8})$$

Substituting Eqs. (A.6) and (A.7) into Eq. (A.8) yields

$$\begin{aligned}
\rho_p &= \frac{\rho_m \rho_{mo}}{s \rho_m + (1-s) \rho_{mo}} + \frac{(\rho_m - \rho_{mo}) s \rho_m}{s \rho_m + (1-s) \rho_{mo}} \frac{V_0}{V_p} \\
&= \frac{\rho_{mo}}{s + (1-s) \rho_{mo} / \rho_m} + \frac{(\rho_m - \rho_{mo}) s}{s + (1-s) \rho_{mo} / \rho_m} \frac{V_0}{V_p}
\end{aligned} \tag{A.9}$$

Now let's define a dimensionless parameter, oxide-to-metal density ratio:

$$\varrho := \frac{\rho_{mo}}{\rho_m}. \tag{A.10}$$

Introducing another dimensionless parameter, diameter expansion ratio of the particle:

$$\epsilon := \frac{d_1}{d_0} = \sqrt[3]{\frac{m_1 / \rho_{mo}}{m_0 / \rho_m}} = \sqrt[3]{\frac{\mathcal{M}_{mo} / x}{\mathcal{M}_m} \frac{1}{\varrho}}, \tag{A.11}$$

with d_1 the particle diameter at burnout, \mathcal{M}_m the molar mass of the metal, ϱ also reads

$$\varrho = \frac{1}{\epsilon^3} \cdot \frac{\mathcal{M}_{mo}}{x \mathcal{M}_m} = \left(\frac{d_0}{d_1} \right)^3 \frac{\mathcal{M}_{mo}}{x \mathcal{M}_m}. \tag{A.12}$$

Equation (A.12) allows us to determine ϱ by measuring the diameter expansion ration, ϵ . Therefore, estimating the densities of liquid metals and liquid oxides becomes unnecessary if they are not known *a priori*. However, the oxidation state at burnout is still needed, which may be clear for some metals, such as FeO for iron at approximately the end of diffusion-limited combustion. Then substituting Eq. (A.10) into Eq. (A.9) gives:

$$\rho_p = \frac{\rho_{mo}}{s + (1-s) \varrho} + \frac{(\rho_m - \rho_{mo}) s}{s + (1-s) \varrho} \frac{V_0}{V_p} \tag{A.13}$$

Assuming that the particle remains spherical during oxidation, the particle volume then expresses as:

$$v_p = \frac{\pi}{6} d_p^3. \tag{A.14}$$

Therefore, the particle density as a function of diameter reads

$$\begin{aligned}
\rho_p &= \frac{\rho_{mo}}{s + (1-s) \varrho} + \frac{(\rho_m - \rho_{mo}) s}{s + (1-s) \varrho} \left(\frac{d_0}{d_p} \right)^3 \\
&= \rho_1 + \rho_2 \left(\frac{d_0}{d_p} \right)^3,
\end{aligned} \tag{A.15}$$

with

$$\rho_1 := \frac{\rho_{\text{mo}}}{s + (1 - s)\varrho}, \quad (\text{A.16})$$

and

$$\rho_2 := \frac{(\rho_{\text{m}} - \rho_{\text{mo}})s}{s + (1 - s)\varrho}. \quad (\text{A.17})$$

Although Eq. (A.15) has been obtained previously by Hazenberg [18], the alternative derivation procedure elaborated here is new and more straightforward.

Appendix B. Composition of multi-species gas at the film layer

When only two gaseous species (i.e., oxygen and inert gas) exist, the gas composition in the film layer can be easily determined using Eq. (7). When several inert species present, the determination of the gas composition in the film is a bit complicated (we only consider the situation where only one kind of oxidizer exists). To accomplish this task, we first define a mean molar mass of inert species:

$$\overline{\mathcal{M}}_I := \frac{\sum_{j \neq j_O}^N X_j \mathcal{M}_j}{\sum_{j \neq j_O}^N X_j}, \quad (\text{B.1})$$

where N is the number of species and j_O is the index of the oxygen. As the molar ratios between inert species are constant, $\overline{\mathcal{M}}_I$ is constant too, provided that the diffusivities of all the inert species are identical. At the film layer, the mass fraction of the oxygen can be formulated with $\overline{\mathcal{M}}_I$:

$$Y_{\text{O},f} = \frac{X_{\text{O},f} \mathcal{M}_O}{X_{\text{O},f} \mathcal{M}_O + (1 - X_{\text{O},f}) \overline{\mathcal{M}}_I}. \quad (\text{B.2})$$

Rearranging Eq. (B.2) yields the molar fraction of the oxygen at the film layer:

$$X_{\text{O},f} = \frac{Y_{\text{O},f} \overline{\mathcal{M}}_I}{Y_{\text{O},f} \overline{\mathcal{M}}_I + (1 - Y_{\text{O},f}) \mathcal{M}_O}. \quad (\text{B.3})$$

The molar fractions of inert species are then can be determined as

$$X_{j,f} = (1 - X_{\text{O},f}) \frac{X_{j,\infty}}{\sum_{j \neq j_O}^N X_{j,\infty}}, \quad j \in [1, N] \ \& \ j \neq j_O. \quad (\text{B.4})$$

Finally, $\lambda_f = \lambda(T_f, X_f)$, $(\rho_g \mathcal{D}_O)_f = \rho_g(T_f, X_f) \mathcal{D}_O(T_f, X_f)$, $c_{p,f} = c_{p,g}(T_f, X_f)$, and $c_{p,O} = c_{p,O}(T_f)$ are determined. X_f is the array of the molar fractions of all gaseous species at the film layer.